Global and local characterization explains the different mechanisms of failure of the human ribs

Published Version:
Palanca M., Liebsch C., Hubner S., Marras D., Ruspi M.L., Marconi F., et al. (2022). Global and local characterization explains the different mechanisms of failure of the human ribs. JOURNAL OF THE MECHANICAL BEHAVIOR OF BIOMEDICAL MATERIALS, 125, 1-9 [10.1016/j.jmbbm.2021.104931].

Availability:
This version is available at: https://hdl.handle.net/11585/841838 since: 2021-12-15

Published:
DOI: http://doi.org/10.1016/j.jmbbm.2021.104931

Global and local characterization explains the different mechanisms of failure of the human ribs.

Palanca M, Liebsch C, Hübner S, Marras D, Ruspi ML, Marconi F, Cristofolini L, Wilke HJ.

J Mech Behav Biomed Mater. 2022 Jan;125:104931.

doi: 10.1016/j.jmbbm.2021.104931. Epub 2021 Oct 28.

Global and local characterization explains the different mechanisms of failure of the human ribs

Marco Palanca[1,2,3], Christian Liebsch[4], Shamila Hübner[4], Daniele Marras[3], Maria Luisa Ruspi[3], Francesco Marconi[3], Luca Cristofolini[3*], Hans-Joachim Wilke[4]

LC and H-J W share the co-senior authorship

[1] Department of Oncology and Metabolism, University of Sheffield, Sheffield, UK

[2] INSIGNEO Institute for in silico medicine, University of Sheffield, Sheffield, UK

[3] Department of Industrial Engineering, Alma Mater Studiorum – Università di Bologna, Bologna, Italy

[4] Institute of Orthopaedic Research and Biomechanics, Trauma Research Center Ulm (ZTF), University Hospital Ulm, Ulm, Germany

*Corresponding author:
Email: luca.cristofolini@unibo.it

Department of Industrial Engineering, Alma Mater Studiorum – Università di Bologna, Via Umberto Terracini 24-28, 40131 Bologna, Italy

Abstract

Knowledge of the mechanics and mechanistic reasons inducing rib fracture is fundamental for forensic investigations and for the design of implants and cardiopulmonary resuscitation devices. A mechanical rationale to explain the different rib mechanisms of failure is still a challenge. The aim of this work was to experimentally characterize human ribs to test the hypothesis that a correlation exists between the ribs properties and the mechanism of failure. 89 ribs were tested in antero-posterior compression. The full-field strain distribution was measured through Digital Image Correlation. The fracture load ranged 7 - 132 N. Two main different mechanisms of failure were observed: brittle and buckling. The strain analysis showed that the direction of principal strains was either aligned with the ribs, or oblique, around 45°, with a rather uniform direction in the most strained area. The maximum principal strains were in the range between 1000 and 30000 microstrain and the minimum principal strain between -30000 and -800 microstrain. The ribs undergoing brittle fracture had significantly thicker cortical bone than those undergoing buckling. Also, larger tensile strains were observed in the specimens with brittle fracture than in the buckling ones. These findings support the focus of cortical thickness modelling which could help in sharpening computational models for the aforesaid purposes.

Keywords:

human ribs, in vitro biomechanical tests, mechanism of failure, fracture pattern, strain analysis, digital image correlation

Introduction

Rib fractures occur within a wide range of accident types. These accidents include falls or collisions which involve blunt chest trauma, or are the unwanted side-effect of emergency operations, (e.g. cardiopulmonary resuscitation), or are the result of traffic accidents (Brasel et al., 2006; Duma et al., 2011; Liebsch et al., 2019b; Nirula and Mayberry, 2010). Due to the high incidence of rib fractures and the associated high rates of mortality and morbidity (Kent et al., 2008), deformability and fragility of the ribs is studied by the scientific community from various perspectives (Kang et al., 2021; Liebsch and Wilke, 2018; Pezowicz and Glowacki, 2021). A better understanding of the mechanical behaviour of the ribs would be important for basic science (e.g.: improve the modelling strategy) but also for clinical purposes. In fact, a deep knowledge of the mechanical behavior of the ribs could aid in the design of better safety devices and improve the reconstruction of traumatic events in the forensic field (Campbell et al., 2009; Daegling et al., 2008; Kang et al., 2021; Mohr et al., 2007).

In vitro experiments were performed to characterize ribs mechanical behaviour and their fracture mechanism. Three-point bending and antero-posterior compression tests were used to characterize the material properties as well as the structural biomechanical response of ribs (Harden et al., 2019; Iraeus et al., 2020; Li et al., 2010a; Liebsch et al., 2021; Love and Symes, 2004; Pezowicz and Glowacki, 2021; Yoganandan and Pintar, 1998). Moreover, subject-specific anatomical and morphological factors, such as the rib level, the cortical thickness and the bone mineral density, were found to play a fundamental role for the fragility of the ribs, and thus for the prediction of possible failures (Harden et al., 2019; Holcombe et al., 2019, 2018; Kemper et al., 2007; Liebsch et al., 2021). By contrast, age, sex, and height were found to play minor roles in rib fragility (Harden et al., 2017; Liebsch et al., 2021).

More complex is the definition of the fracture patterns and of the mechanisms of failure. A first analysis and classification of the fracture patterns was performed in a retrospective study with almost 500 ribs, mostly harvested during autopsy (Love and Symes, 2004). This study, with a forensic motivation, described four patterns of fracture (transverse, oblique, butterfly, and buckle) and showed the lack of systematic correlation with age, sex, and ancestry. Moreover, the authors clearly underlined how the ribs' failure point seemed to contradict the bone biomechanics literature. Indeed, it is well known that bone is stronger in compression and weaker in tension (Bayraktar et al., 2004; Keaveny et al., 1994; Reilly and Burstein, 1975). However, (Love and Symes, 2004) repeatedly observed failures at the points of compression prior to points of tension. The same clinically relevant fracture patterns were replicated *in vitro* (Daegling et al., 2008; Harden et al., 2019), where fracture loads and point-wise strains, using strain gauges, were measured. While the tests simulated clinically relevant fracture of the ribs, a mechanistic rationale to explain the different patterns of fracture was not outlined.

The work of Love and Symes (2004) also identified two possible mechanisms of failure: brittle and buckling. While elderly bones (more brittle) are less likely to exhibit plastic response to loading, a high-strain (buckling) failure is expected in young bones (Agnew et al., 2014). However, rib properties that preliminary indicate which mechanisms of failure could be expected have not yet been identified.

Finite element models were developed to better understand rib responses to different impact loads together with the growing experimental biomechanical knowledge. In fact, the great amount of experimental data allowed to generate more biofidelic models and to refine their prediction. Both in generic (Iraeus et al., 2020; Wang et al., 2016) and subject-specific (Iraeus et al., 2019; Li et al., 2010a, 2010b) finite element models, the predicted fracture load, stiffness, and strain values were validated against experimental data. However, the prediction of the fracture onset location and the mechanisms of failure remain a challenge.

In this context, a study that matches anatomical and morphometric details with a comprehensive biomechanical characterization of the strain field to describe the possible cause-effect relations is still missing.

This study provides a comprehensive characterization of human ribs in terms of global behaviour of the different ribs (e.g. failure load, rib level), and of local properties (e.g. strain pattern, and cortical thickness at the location of fracture onset). Therefore, the purpose of this study was to test the hypothesis that the global behaviour and local properties explain the mechanism of failure.

Material and methods

Sample preparation

The same sample that was used in the study of (Liebsch et al., 2021) to identify the anthropometric factors that promote rib fragility was used in the present study. The sample consisted of 89 fresh frozen ribs from 13 donors, from levels 4 to 8 (Table 1). Specimens were obtained through an ethically-approved donation program; the entire study was approved by the ethics committee of the University of Ulm (vote no. 92/20).

The ribs were isolated from the spines (vertebral extremity) by carefully cutting the ligaments and removing the muscles, and anteriorly (sternal extremity) by cutting the costal cartilage. The periosteum was removed using fine sandpaper, taking care not to damage the periosteal cortical shell. The vertebral and sternal extremities of the ribs were embedded in poly-methyl-methacrylate (Technovit 3040, Heraeus Kulzer, Germany) for a length of about 40 mm to guarantee a stable fixation with the testing setup. The ribs were frozen in sealed bags when not in use and thawed the night before the test in physiological saline solution.

Before the tests, rib surfaces were sprayed with a thin layer of white water-based paint and then with a black random speckle pattern (Lionello and Cristofolini, 2014; Palanca et al., 2015) to allow Digital Image Correlation (DIC) measuring the strains.

Table 1: Summary of the donors' details and ribs tested. The letter "C" indicates that the strain analysis was performed on the cutaneous surface; "P" on the pleural surface.

			Rib level									
			Right					Left				
Donor	Age (y)	Sex	4	5	6	7	8	4	5	6	7	8
1	55	F					**P**					**C**
2	62	M	**C**	**P**	**C**	**P**	**C**	**P**	**C**	**P**	**C**	**P**
3	63	M	**P**	**C**		**P**	**C**	**C**	**P**		**C**	**P**
4	64	F				**C**	**P**			**C**	**P**	**C**
5	65	F							**C**	**P**		**C**
6	68	M	**P**	**C**	**P**	**C**	**P**	**C**	**P**	**C**	**P**	**C**
7	71	F		**P**		**P**	**P**	**P**	**C**		**P**	**C**
8	80	M	**P**	**C**	**P***	**C**	**P**	**C**	**P**	**C***	**P**	**C**
9	81	M	**C***	**P**		**P**	**P**	**C***	**P**		**C**	**C**
10	84	F	**C**	**P**	**C**	**P**	**C***	**P**	**C**	**P**	**C**	
11	91	M	**P**	**C**		**C**	**P**	**P**	**C**			
12	96	M	**P***	**C**		**P**	**C**	**C**	**P**		**C**	**P**
13	99	F	**P**			**C**					**C**	

* no DIC data available

Biomechanical testing

A uniaxial testing machine (Z010, Zwick Roell AG, Germany) equipped with a 200 N load cell was used. The sternal and vertebral extremities were fixed, respectively, in an adjustable cardan joint to the testing machine crosshead and in a ball-joint to the testing machine frame (Fig. 1). After the alignment of the rib extremities to the loading axis of the testing machine, the ball-joint was locked while the sternal extremity was left free for rotations around the transversal axis of the rib (cardan joint). Each rib was preloaded at 5 N, to reduce the plays between the mechanical components of the loading system, and a monotonic antero-posterior compression was applied, with a speed of 1 mm/s, up to failure. Load and displacement were recorded by the computer of the testing machine at 100 Hz.

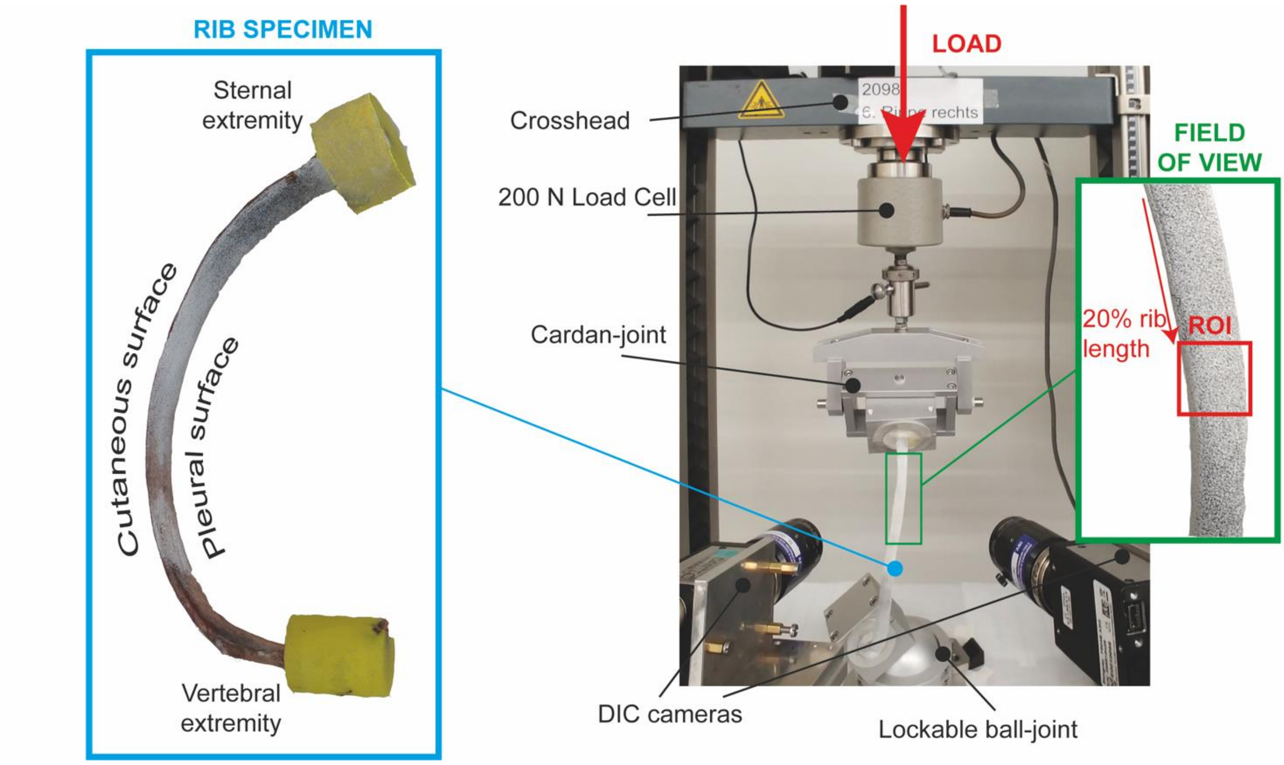

Fig. 1: Illustration of the test setup. The ribs were compressed in antero-posterior direction using a uniaxial testing machine. The sternal extremity (anterior) of the ribs was fixed to an unconstrained cardan joint, whereas the vertebral extremity (posterior) was fixed to a locked ball-joint. A field of view of 100x30 mm was acquired by the two DIC cameras. Within the field of view, a region of interest (ROI) was defined at the 20% of the rib length from the sternal extremity. In the picture on the right, a region of interest (ROI) on the cutaneous surface is reported. A similar region of interest was defined on the pleural surface in those ribs with pleural field of view.

The strain fields of the ribs were evaluated with a 3D-DIC (Q400, Dantec-Dynamics, Skovlunde, Denmark), synchronized with the testing machine. The system consisted of 2 cameras (5MPixels, 2440x2050 pixels, 8-bit, black-and-white) with high-quality metrology-standard 35 mm lens (Xenoplan, Schneider-Kreuznach, Germany) and a directional system of LEDs (10’000 lumens in total). The hardware and software settings (Table 2) were optimized, similar to (Palanca et al., 2015, 2018).

Table 2: Summary of lens data and DIC parameters.

DIC settings	Value
Aperture	f/16
Shutter time	1/50 s
Frame rate	10 Hz
Pixel size	0.03 mm
Facet size	25-39 pixels
Grid spacing	11-17 pixels
Filter	Kernel 9x9

In order to provide a complete characterization of the strain patterns on the ribs, 45 ribs were addressed for strain measurements on the cutaneous surface, while the other 44 were chosen for measurement on the pleural surface. A field of view of 100x30 mm, with a consequent pixel size of 0.03 mm, was chosen to get a global quantitative description of the rib strain patterns. This field of view was chosen as a compromise between the spatial resolution, small enough to catch the local behavior of the rib (Palanca et al., 2015), and the framing, large enough to catch the rib fracture.

In addition, medians of the principal strains were computed on a squared region of interest (ROI) within the DIC field of view for comparison between the different ribs. The ROI was localized at the 20% of the rib length from the sternal extremity, with a dimension like the outer/inner cortex on the cutaneous/pleural field of view (Table 1), since fractures due to antero-posterior compression mostly happen in the anterior one third (Yang et al., 2011).

Assessment of bone quality and bone morphology

None of the specimens had signs of bony defects, fracture, or degeneration.

The bone quality of the ribs was indirectly assessed evaluating the bone mineral density (BMD) of the respective spine in L2, L3 and L4 vertebral bodies by means of a quantitative computed tomography (Somatom Definition AS, Siemens Healthcare, Erlangen, Germany) with an integrated density-reference phantom (Osteo Phantom, Siemens Healthineers, Erlangen, Germany). According to the manufacturer’s instructions, the spine was scanned with a voltage of 80 kVp and a current of 105 mAs, obtaining a voxel size of 0.87x0.87x0.6 mm. The standardized software protocol segmented the trabecular bone of the L2, L3 and L4 vertebral bodies, averaged the attenuation values in Hounsfield Unit (HU) over the three vertebrae, and estimated the volumetric BMD through a HU-to-BMD conversion equation (Baum et al., 2011; Löffler et al., 2019).

Micro-CT scans (Skyscan 1172 Micro-CT, Skyscan, Kontich, Belgium) were performed to evaluate the cortical thickness of each rib, in about 10 mm long samples cut posteriorly from the fracture site. The ribs were scanned with the following energetic parameters: 100 kVp, 100 μAs, with an Al-Cu filter, obtaining an isotropic voxel size of 5 μm. The scanner manufacturer software CTAn (v 1.17.7.2, Skyscan, Kontich, Belgien) was used for the microstructural analysis: the images were segmented using a standard single threshold approach for grayscale values in combination with a calibration phantom (Bruker MicroCT, Kontich, Belgium). The cortical thickness was measured on a volume of interest of 50 adjacent sample slices. For each slice, the average radial thickness (distance between the endosteum and periosteum surfaces) was measured. Then, the thickness value for the each rib was defined as the minimum thickness of the volume of interest.

Metrics and statistical analysis

Each rib was mechanically characterized at fracture evaluating:

- the fracture load: the maximum force measured during the destructive test;
- the median of the maximum principal strain above the cutaneous/pleural ROI;
- the median of the minimum principal strain above the cutaneous/pleural ROI;
- the principal strain alignment above the field of view (Fig. 2): as the principal strains were either aligned close to the ribs axis, or approximately at 45°, the principal strain direction evaluated in the ROI was categorized either as “aligned” (when the average angle was smaller than 20° from the axis) or as “oblique” (when the average angle was in the range 20° - 45°);
- the mechanism of failure (Fig. 3), which was categorized into:
    - Brittle: the fracture was complete and sharp, with failure starting from the cutaneous surface due to tensile strain,
    - Buckling: the fracture was incomplete, and the rib behaved as a hollow pipe, with failure starting from the pleural surface due to compressive strain.

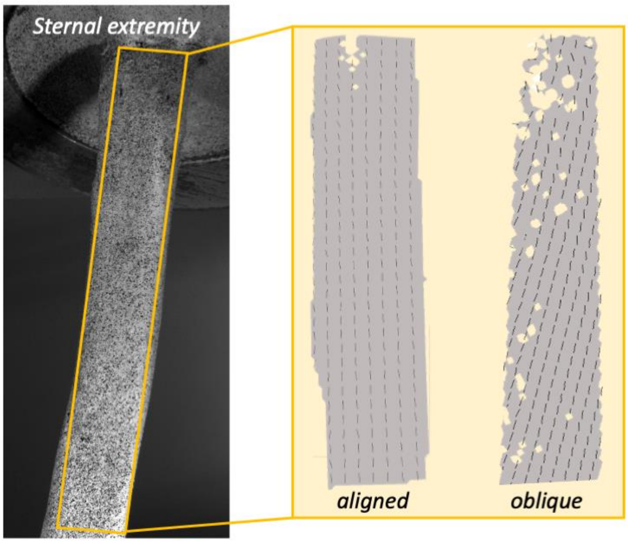

Fig. 2: Principal strain direction was oriented in two distinct ways: aligned with the ribs or oblique, around 45°, with respect to the rib.

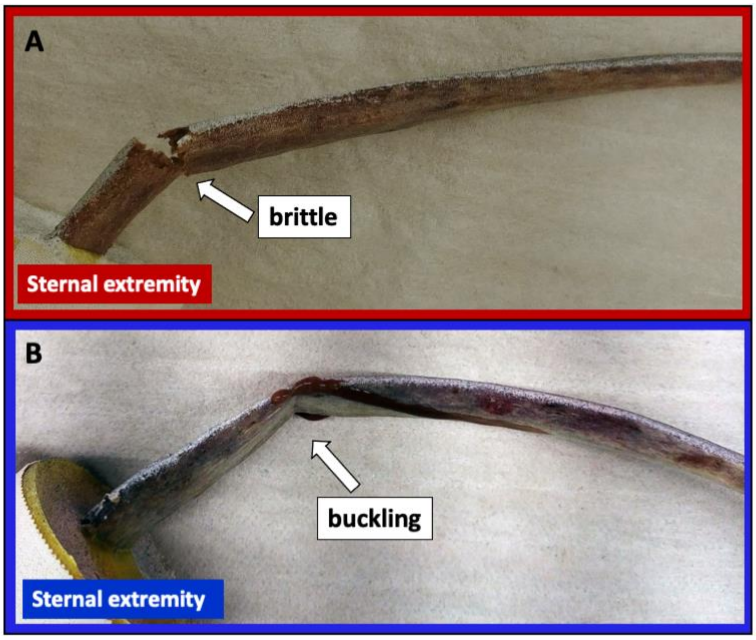

Fig. 3: The two mechanisms of failure observed: brittle (A) and buckling (B).

The correlations of the ribs levels with respect to the maximum principal strains and the minimum principal strains were explored. Normality of the distributions was assessed with the Shapiro-Wilk test. If data met the normality criterion ($p>0.05$), a parametric one-way ANOVA was performed, followed by a Tukey's multiple comparison. Otherwise, a non-parametric Kruskal-Wallis test with a Dunn's multiple comparison was applied.

The characterization was extended to the mechanism of failure mode and to the strain direction. To evaluate if a mechanism of failure and a strain alignment were typical for a specific rib level, the Chi-

square test was used. In addition, as the ribs were categorized in terms of mechanism of failure (buckling or brittle) and of principal strain alignment (aligned or oblique), the possible association between mechanism of failure and strain alignment was assessed with the Fisher's exact test.
Finally, the possible association of the mechanism of failure with the failure load, with the maximum principal strains, with the minimum principal strains, and with the cortical thickness in the retrospective failure section were explored. In the last case, due to the physiological differences in terms of ribs dimensions among the different levels of the ribs, a normalization of the rib cortical thickness was performed. The mean cortical thickness for each rib level was evaluated as the average of the cortical thickness in the closeness of the fracture among the ribs of such level. Then, the normalized cortical thickness was computed for each rib, as the ratio between the measured cortical thickness of that rib, and the mean cortical thickness at that level. The normality of distributions was tested with the Shapiro-Wilk test. If the sample passed the normality test, the association were tested with an unpaired t-test, otherwise a Mann-Whitney test was used to compare the ranks.
All statistical analyses were performed with Prism 8 (GraphPad Software, USA), using a level of statistical significance at 0.05.

Results

All ribs showed a qualitatively similar load-displacement trend: quasi-linear in the initial phase and followed by a non-linear phase with decreasing slope, ending with an abrupt force drop (Fig. 4).

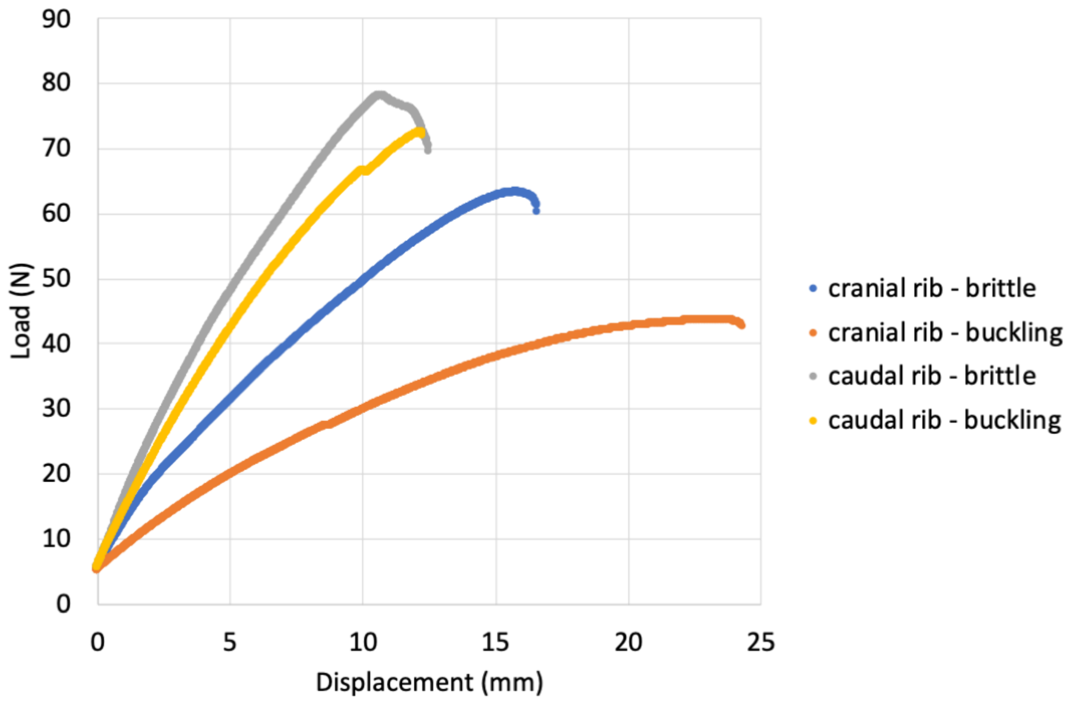

Fig. 4: Typical load-displacement curves of cranial and caudal ribs with a brittle and buckling mechanism of failure. The rib was pre-loaded at 5 N (initial point), then a monotonic compression up to failure (force drop) was applied. In blue data from donor 3, rib 4 left; in orange data from donor 6, rib 4 left; in grey data from donor 3, rib 7 right; and in yellow data from donor 2, rib 7 left.

The majority of the ribs showed simple fracture patterns (85/89), in particular 60 transverse and 25 oblique fractures, while the remaining 4 ribs showed multi-fragmentary fracture pattern, according to the AO/OTA fracture classification (Meinberg et al., 2018). The onset fracture location in 88 cases out of 89 cases was in the 25% of the rib length from the sternal extremity, while just one specimen fractured close to the vertebral extremity.

The fracture load ranged between 7.3 N (donor: 13, rib: 7 right) and 132 N (donor: 3, rib: 7 right), with a coefficient of variation equal to 40% (SD/mean), as reported also in (Liebsch et al., 2021).

83 ribs (41 analyzed on the cutaneous surface and 42 analyzed on the pleural surface) were considered for the strain analysis, 6 out of 89 ribs were excluded due to poor DIC correlation. The analysis of the DIC-measured strains showed a systematic error of 20 microstrain and a random error of 60 microstrain. The global quantitative characterization of the ribs showed a homogeneous strain distribution, with no obvious strain concentrations, for both the cutaneous and pleural ROI, for both the maximum and the minimum principal strain (Fig. 5). The direction of the principal strains was aligned in 50 ribs and oblique in 31 ribs (Fig. S2). The principal strain direction was not identified in two cases (donor: 10, rib: 4 right; donor: 12, rib: 5 right) which were excluded.

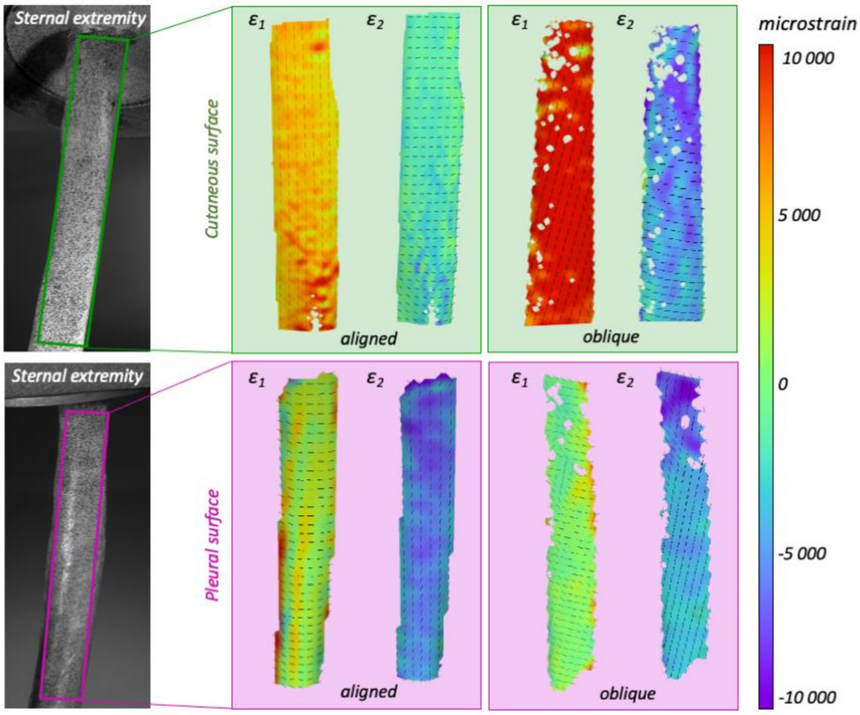

Fig. 5: Maximum (ε_1) and minimum (ε_2) principal strains measured by the DIC on the field of view of the cutaneous surface (top green boxes) and pleural surface (bottom purple boxes) of the ribs immediately before failure. Each box represents a different rib. The dashes overlayed on the strain maps show the direction of the principal strains: they were either roughly aligned with the rib ("aligned"), or at 45° ("oblique").

The maximum principal strains above the ROI on the cutaneous surface ranged between 1000 microstrain (donor: 10, rib: 4 right) and 30000 microstrain (donor: 8, rib: 5 right), while on the pleural surface it ranged between -3900 microstrain (donor: 12, rib: 7 right) and 2300 microstrain (donor: 6, rib: 7 left). The minimum principal strains above the ROI on the cutaneous surface ranged between -6200 microstrain (donor: 12, rib: 8 right) and -100 microstrain (donor: 9, rib: 7 left), while on the pleural surface, it ranged between -30000 microstrain (donor: 9, rib: 7 right) and -800 microstrain (donor: 6, rib: 5 left)(Fig. 6).

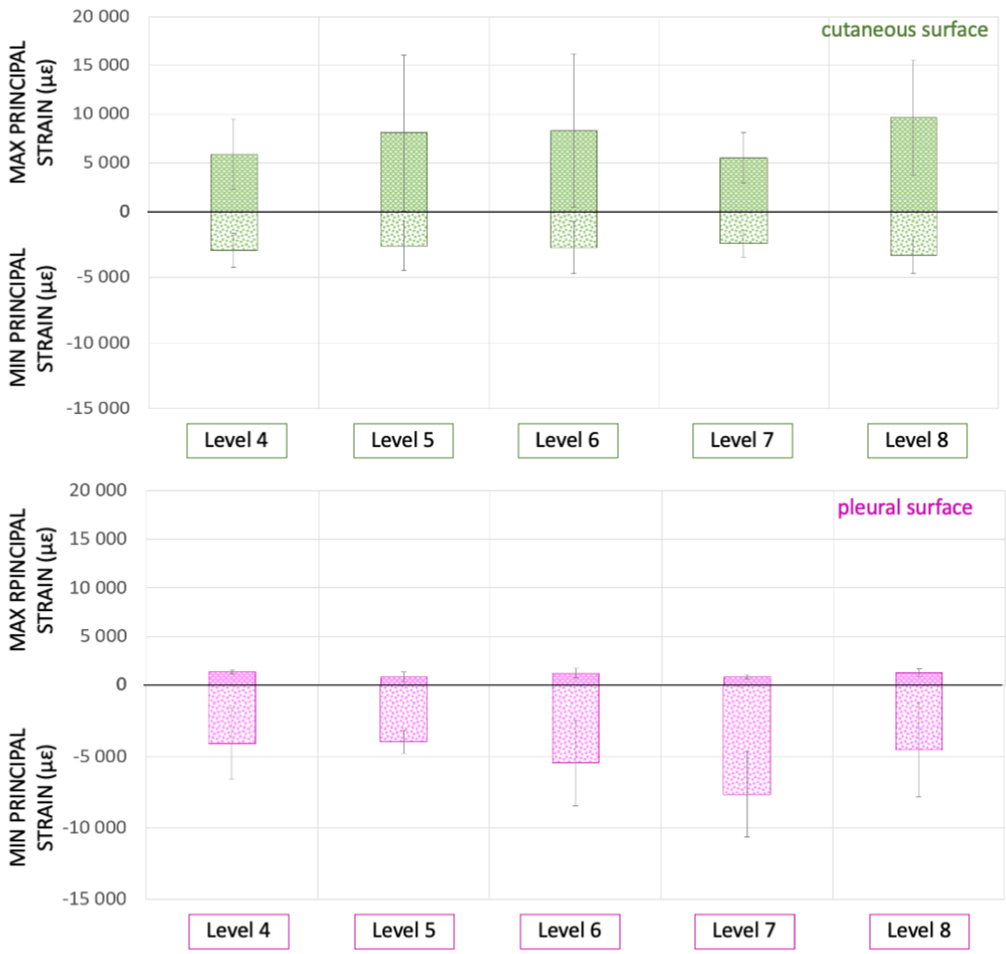

Fig. 6: Maximum and minimum principal strain measured by the DIC on the ROI of the cutaneous surface (top, green) and on the pleural surface (bottom, purple) of the ribs immediately before failure. The mean and standard deviations among the ribs at each level are plotted.

Two mechanisms of failure were observed: the buckling mechanism (n=35/89), where collapse initiated by inwards folding on the pleural cortex under compressive strains and the brittle mechanism (n=42/89), where the collapse was clear-cut (Fig. 3). In twelve cases, the mechanism of failure was not clear, because it resulted in a mix of the two principals.

No significant differences were observed for the principal strains at the different rib levels (Fig. 6) (Kruskal-Wallis, see table 3 for the p-values).

No correlation existed between the mechanism of failure and the rib level (Chi-square test, p-value = 0.492) as well as between the strain direction and the rib level (Chi-square test, p-value = 0.866).

No dichotomy existed between the mechanism of failure and the principal strain direction (Fig. S3, Fisher's exact test, p-value = 0.639).

The fracture loads were similar in case of brittle or buckling mechanism of failure (Mann-Whitney test, p-value = 0.136). The maximum principal strains on the cutaneous surface were significantly larger (Mann-Whitney test, p-value = 0.005) in the specimens failed with a brittle mechanism than those with a buckle mechanism. By contrast, no trend was observed between the mechanism of failure and the minimum principal strain (Mann-Whitney test, p-value = 0.700). No trends were observed also between the mechanism of failure and the maximum and minimum principal strains (Mann-Whitney test; respectively, p-value = 0.700 and p-value=0.140) on the pleural surface. The specimens that fractured in brittle mechanism systematically showed thicker cortical layer (unpaired t-test, p-value = 0.042) (Fig. 7 and Table 3).

Table 3: Overview of the significance of the effects and correlations. The physical entities compared are listed in the first column. The statistical test and the p-values are reported in the following columns. The last column points to the illustration in the main paper or in the Supplementary Material (SM) where each comparison can be found. The data for the statistical tests were collected in the Supplementary Material (Table S1). Each sheet contains the data for each test reported in Table 3.

Analysis	**Statistical test**	**p-value**	**Figure**
Rib level vs eps max (cutaneous surface)	Kruskal-Wallis	0.431	Fig. 5
Rib level vs eps max (pleural surface)	Kruskal-Wallis	0.728	Fig. 5
Rib level vs eps min (cutaneous surface)	Kruskal-Wallis	0.705	Fig. 5
Rib level vs eps min (pleural surface)	Kruskal-Wallis	0.460	Fig. 5
Rib level vs mechanism of failure	Chi-square	0.492	SM, Fig. S1
Rib level vs strain direction	Chi-square	0.866	SM, Fig. S2
Mechanism of failure vs strain direction	Fisher's exact test	0.639	SM, Fig. S3
Mechanism of failure vs load	Mann-Whitney	0.136	Fig. 7
Mechanism of failure vs eps max (cutaneous surface)	Mann-Whitney	0.005 *	Fig. 7
Mechanism of failure vs eps max (pleural surface)	Mann-Whitney	0.700	Fig. 7
Mechanism of failure vs eps min (cutaneous surface)	Mann-Whitney	0.127	Fig. 7
Mechanism of failure vs eps min (pleural surface)	Mann-Whitney	0.140	Fig. 7
Mechanism of failure vs normalized cortical thickness	Unpaired t-test	0.042 *	Fig. 7

* indicates statistical significance.

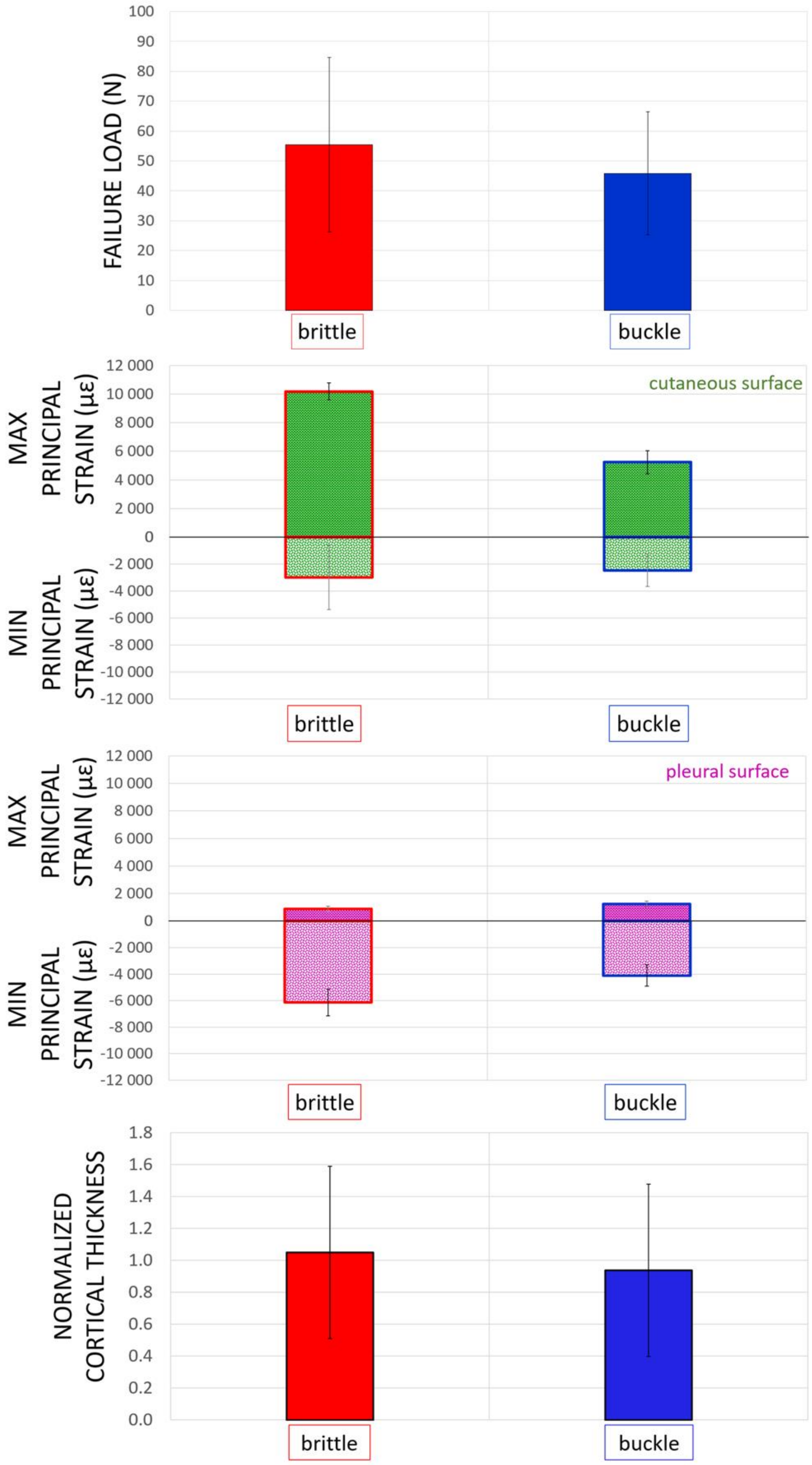

Fig. 7: Failure load, maximum and minimum principal strain on the ROI of the cutaneous and pleural surface, and normalized cortical thickness for the two mechanisms of failure (brittle and buckling). The maximum principal strain on the cutaneous surface and the normalized cortical thickness were systematically larger in those specimens that fractured in brittle mechanism.

Discussion

The aim of this work was to provide a comprehensive characterization of the ribs in terms of failure load, mechanism of failure, and strain field at failure. We tested the hypothesis that correlations exist between global and local rib properties and the mechanism of failure.

A series of 89 ribs from 13 cadavers were tested in antero-posterior compression to replicate a fundamental component of the complex load which the ribs usually experience in case of severe thoracic compression (e.g. in cardio-pulmonary resuscitation or loading by occupant restraint systems).

Fracture patterns, load/displacement curves, and measured fracture loads were consistent with the ones showed by (Daegling et al., 2008; Yang et al., 2011), confirming the validity of this *in vitro* experiment. The fracture location, close to the sternal extremities, and the simple fracture pattern, with transverse and oblique fractures, replicated the fracture appearance observed in actual cases by (Harden et al., 2019). High variability in terms of fracture loads was found as a consequence of the different factors (i.e. rib morphology, bone mineral density) that (Liebsch et al., 2021) found leading to fracture. Nevertheless, homogeneous strain patterns with similar strain magnitudes were observed both in the cutaneous and pleural sides of the ribs. The strain patterns confirm the optimization of the rib structure for this loading scenario, as (Cristofolini, 2015) showed for other bones loaded in physiological conditions.

Two different strain directions (either aligned with the rib, or oblique around 45°) were observed on the surface of the ribs, while a clear correlation with other parameters was not found in the present study. We hypothesize that a torsion component was introduced in some ribs by the intrinsic shape of the ribs itself that leans the direction of the principal strains measured on the cutaneous or pleural surface.

Regardless of the fracture pattern, two different mechanisms of failure were observed. Statistically significant differences were found between the two mechanisms of failure in relation to the maximum principal strain on the cutaneous surface: the maximum principal strains on the cutaneous surface, immediately before failure, were significantly higher in the specimens that underwent brittle failure than in those with buckle. This confirmed the existence of the brittle and buckling mechanisms driven by two different mechanical events (Love and Symes, 2004). A possible explanation could be attributed to the combined effect of the cortical thickness and of the loading scenario which the ribs undergo. The brittle failure of the ribs seems to be regulated by the maximum principal strain, which typically happens in thick cortical bones (i.e. the medial and medial-posterior sides of the femoral neck in physiological loading direction fail in tension like a brittle material) (Tang et al., 2018). By contrast, the buckling mechanism observed in thin cortical bones (i.e. the lateral cortex of the femoral neck, which is similar to the ribs' cortical thickness, in sideways fall condition fails in compression) seemed to be driven by cortical instability due to compressive stress. Analyses of the microcracking patterns could confirm at the microscale what we observed at the macroscale (Tang et al., 2018).

The failures of the ribs in tension region confirmed the different behaviour of the ribs with respect to other bones, as observed by (Love and Symes, 2004). This is highlighted also by the study of (Albert et al., 2021) on the ribs cortical tissue, which showed yield strains larger in compression than in tension, but ultimate strains smaller in compression than in tension, both for slow (i.e. 0.005 strain/s) and fast (i.e. 0.5 strain/s) loading rate.

No significant difference in the fracture load was found between the groups with brittle and with buckling fracture. As explained in previous works, the cortical thickness plays a fundamental role in promoting rib fragility (Holcombe et al., 2019; Liebsch et al., 2021). In the present study, thin cortical thickness of the ribs loaded in antero-posterior direction induced buckling. This effect was confirmed by the significant difference between the cortical thickness of the ribs fractured in brittle mechanism (thicker) and the ones fractured in buckling mechanism (significantly thinner). In this respect, different loading conditions (i.e. the loads induced by automotive belt) may induce different mechanisms of failure.

To the authors' knowledge, a rationale to explain the two different mechanisms of failure of the rib was not developed yet and could be an interesting parameter to focus on in case of numerical modelling for forensic purposes. Indeed, several computational works reported the difficulty in accounting for the mechanism of failure (Iraeus et al., 2020; Li et al., 2010b, 2010a). The experimental evidence obtained in this work, as well as in (Liebsch et al., 2021), stresses the importance of the cortical thickness in the rib mechanism of failure. This supports the application of dedicated numerical tools (Iraeus et al., 2020, 2019), as the cortical bone mapping (Holcombe et al., 2018), to better discriminate the cortical thickness also from clinical CT images. A simplified evaluation of the cortical thickness may be sufficient, instead, if the aim is to estimate the fracture load or the strain field (Li et al., 2010a).

The loading condition implemented in the present study was a simplification compared with the complex loading conditions experienced during a high-energy trauma or a fall. However, although antero-posterior compression is not the one and only load component acting on the ribs, it is one of the most relevant components (Liebsch et al., 2019a). Furthermore, as traumatic events are highly variable and scarcely predictable, it would be impossible to define a unique complex loading scenario. For this reason, a simplified one, yet based on the predominant component of load was chosen, as it is most reproducible. Another limitation of this study could be the relatively low loading rate compared to the loading rate of an actual trauma (Katzenberger et al., 2020). However, the loading rate was chosen to enable accurate strain measurement with DIC. Larger strains could be expected in case of increased loading rate (Albert et al., 2021). However, the loading rate is not likely to have affected the overall findings of the study.

Conclusions

The experimental tests performed on a large sample of ribs allowed to replicate clinically relevant fracture patterns. In particular, the tests confirmed the existence of two specific mechanisms of failure, brittle and buckling. The maximum principal strain field associated with the two mechanisms of failure were significantly different. We showed evidence of the importance of the cortical thickness driving either a brittle or buckling mechanism of failure in the human ribs.

Acknowledgements

This study was funded by the German Research Foundation (DFG, project WI 1352/20-2).

References

Agnew, A., Moorhouse, K., Murach, M., White, S., Kang, Y.-S., 2014. Tensile stress in human ribs throughout the lifespan. IRCOBI conference 2014.

Albert, D.L., Katzenberger, M.J., Agnew, A.M., Kemper, A.R., 2021. A comparison of rib cortical bone compressive and tensile material properties: Trends with age, sex, and loading rate. Journal of the Mechanical Behavior of Biomedical Materials 122, 104668. https://doi.org/10.1016/j.jmbbm.2021.104668

Baum, T., Müller, D., Dobritz, M., Rummeny, E.J., Link, T.M., Bauer, J.S., 2011. BMD measurements of the spine derived from sagittal reformations of contrast-enhanced MDCT without dedicated software. European Journal of Radiology 80, e140–e145. https://doi.org/10.1016/j.ejrad.2010.08.034

Bayraktar, H.H., Morgan, E.F., Niebur, G.L., Morris, G.E., Wong, E.K., Keaveny, T.M., 2004. Comparison of the elastic and yield properties of human femoral trabecular and cortical bone tissue. Journal of Biomechanics 37, 27–35. https://doi.org/10.1016/S0021-9290(03)00257-4

Brasel, K.J., Guse, C.E., Layde, P., Weigelt, J.A., 2006. Rib fractures: Relationship with pneumonia and mortality*: Critical Care Medicine 34, 1642–1646. https://doi.org/10.1097/01.CCM.0000217926.40975.4B

Campbell, N., Conaglen, P., Martin, K., Antippa, P., 2009. Surgical Stabilization of Rib Fractures Using Inion OTPS Wraps—Techniques and Quality of Life Follow-Up. Journal of Trauma: Injury, Infection & Critical Care 67, 596–601. https://doi.org/10.1097/TA.0b013e3181ad8cb7

Cristofolini, L., 2015. In vitro evidence of the structural optimization of the human skeletal bones. Journal of Biomechanics 48, 787–796. https://doi.org/10.1016/j.jbiomech.2014.12.010

Daegling, D.J., Warren, M.W., Hotzman, J.L., Self, C.J., 2008. Structural Analysis of Human Rib Fracture and Implications for Forensic Interpretation*. Journal of Forensic Sciences. https://doi.org/10.1111/j.1556-4029.2008.00876.x

Duma, S.M., Kemper, A.R., Stitzel, J.D., Mcnally, C., Kennedy, E.A., Matsuoka, F., 2011. Rib fracture timing in dynamic belt tests with human cadavers. Clin. Anat. 24, 327–338. https://doi.org/10.1002/ca.21130

Harden, A., Kang, Y.-S., Agnew, A., 2019. Rib Fractures: Validation of an Interdisciplinary Classification System. fa 2, 158–167. https://doi.org/10.5744/fa.2019.1032

Harden, A., Kang, Y.-S., Moorhouse, K., Agnew, A., 2017. Variance in Fracture Location of Human Ribs Subjected to Dynamic Antero-Posterior Bending. IRCOBI conference 2017.

Holcombe, S.A., Hwang, E., Derstine, B.A., Wang, S.C., 2018. Measuring rib cortical bone thickness and cross section from CT. Medical Image Analysis 49, 27–34. https://doi.org/10.1016/j.media.2018.07.003

Holcombe, S.A., Kang, Y., Derstine, B.A., Wang, S.C., Agnew, A.M., 2019. Regional maps of rib cortical bone thickness and cross-sectional geometry. J. Anat. 235, 883–891. https://doi.org/10.1111/joa.13045

Iraeus, J., Brolin, K., Pipkorn, B., 2020. Generic finite element models of human ribs, developed and validated for stiffness and strain prediction – To be used in rib fracture risk evaluation for the human population in vehicle crashes. Journal of the Mechanical Behavior of Biomedical Materials 106, 103742. https://doi.org/10.1016/j.jmbbm.2020.103742

Iraeus, J., Lundin, L., Storm, S., Agnew, A., Kang, Y.-S., Kemper, A., Albert, D., Holcombe, S., Pipkorn, B., 2019. Detailed subject-specific FE rib modeling for fracture prediction. Traffic Injury Prevention 20, S88–S95. https://doi.org/10.1080/15389588.2019.1665649

Kang, Y.-S., Kwon, H.J., Stammen, J., Moorhouse, K., Agnew, A.M., 2021. Biomechanical Response Targets of Adult Human Ribs in Frontal Impacts. Ann Biomed Eng 49, 900–911. https://doi.org/10.1007/s10439-020-02613-x

Katzenberger, M.J., Albert, D.L., Agnew, A.M., Kemper, A.R., 2020. Effects of sex, age, and two loading rates on the tensile material properties of human rib cortical bone. Journal of the Mechanical Behavior of Biomedical Materials 102, 103410. https://doi.org/10.1016/j.jmbbm.2019.103410

Keaveny, T.M., Guo, X.E., Wachtel, E.F., McMahon, T.A., Hayes, W.C., 1994. Trabecular bone exhibits fully linear elastic behavior and yields at low strains. Journal of Biomechanics 27, 1127–1136. https://doi.org/10.1016/0021-9290(94)90053-1

Kemper, A., McNally, C., Pullins, C., Freeman, L., Duma, S., Rouhana, S., 2007. The biomechanics of human ribs: Material and structural properties from dynamic tension and bending tests. Stapp car crash journal 51, 235–73.

Kent, R., Woods, W., Bostrom, O., 2008. Fatality Risk and the Presence of Rib Fractures. Proceedings of advances in automotive medicine 52, 73.

Li, Z., Kindig, M.W., Kerrigan, J.R., Untaroiu, C.D., Subit, D., Crandall, J.R., Kent, R.W., 2010a. Rib fractures under anterior–posterior dynamic loads: Experimental and finite-element study. Journal of Biomechanics 43, 228–234. https://doi.org/10.1016/j.jbiomech.2009.08.040

Li, Z., Kindig, M.W., Subit, D., Kent, R.W., 2010b. Influence of mesh density, cortical thickness and material properties on human rib fracture prediction. Medical Engineering & Physics 32, 998–1008. https://doi.org/10.1016/j.medengphy.2010.06.015

Liebsch, C., Graf, N., Wilke, H.-J., 2019a. In vitro analysis of kinematics and elastostatics of the human rib cage during thoracic spinal movement for the validation of numerical models. Journal of Biomechanics 94, 147–157. https://doi.org/10.1016/j.jbiomech.2019.07.041

Liebsch, C., Hübner, S., Palanca, M., Cristofolini, L., Wilke, H.-J., 2021. Experimental study exploring the factors that promote rib fragility in the elderly. Sci Rep 11, 9307. https://doi.org/10.1038/s41598-021-88800-9

Liebsch, C., Seiffert, T., Vlcek, M., Beer, M., Huber-Lang, M., Wilke, H.-J., 2019b. Patterns of serial rib fractures after blunt chest trauma: An analysis of 380 cases. PLoS ONE 14, e0224105. https://doi.org/10.1371/journal.pone.0224105

Liebsch, C., Wilke, H.-J., 2018. Chapter 3 - Basic Biomechanics of the Thoracic Spine and Rib Cage, in: Galbusera, F., Wilke, H.-J. (Eds.), Biomechanics of the Spine. Academic Press, pp. 35–50. https://doi.org/10.1016/B978-0-12-812851-0.00003-3

Lionello, G., Cristofolini, L., 2014. A practical approach to optimizing the preparation of speckle patterns for digital-image correlation. Measurement Science and Technology 25, 107001. https://doi.org/10.1088/0957-0233/25/10/107001

Löffler, M.T., Jacob, A., Valentinitsch, A., Rienmüller, A., Zimmer, C., Ryang, Y.-M., Baum, T., Kirschke, J.S., 2019. Improved prediction of incident vertebral fractures using opportunistic QCT compared to DXA. Eur Radiol 29, 4980–4989. https://doi.org/10.1007/s00330-019-06018-w

Love, J.C., Symes, S.A., 2004. Understanding Rib Fracture Patterns: Incomplete and Buckle Fractures. J. Forensic Sci. 49, 1–6. https://doi.org/10.1520/JFS2004175

Meinberg, E., Agel, J., Roberts, C., Karam, M., Kellam, J., 2018. Fracture and Dislocation Classification Compendium—2018. Journal of Orthopaedic Trauma 32, S1–S10. https://doi.org/10.1097/BOT.0000000000001063

Mohr, M., Abrams, E., Engel, C., Long, W.B., Bottlang, M., 2007. Geometry of human ribs pertinent to orthopedic chest-wall reconstruction. Journal of Biomechanics 40, 1310–1317. https://doi.org/10.1016/j.jbiomech.2006.05.017

Nirula, R., Mayberry, J.C., 2010. Article Commentary: Rib Fracture Fixation: Controversies and Technical Challenges. The American Surgeon 76, 793–802. https://doi.org/10.1177/000313481007600820

Palanca, M., Brugo, T.M.M., Cristofolini, L., 2015. Use of Digital Image Correlation to Understand the Biomechanics of the Vertebra. Journal of Mechanics in Medicine and Biology 15, 1540004–1540010. https://doi.org/10.1142/S0219519415400047

Palanca, M., Marco, M., Ruspi, M.L., Cristofolini, L., 2018. Full-field strain distribution in multi-vertebra spine segments: An in vitro application of digital image correlation. Medical Engineering & Physics 52, 76–83. https://doi.org/10.1016/j.medengphy.2017.11.003

Pezowicz, C., Glowacki, M., 2021. The mechanical properties of human ribs in young adult. Acta of Bioengineering and Biomechanics 14, 53–50.

Reilly, D.T., Burstein, A.H., 1975. The elastic and ultimate properties of compact bone tissue. Journal of Biomechanics 8, 393–405. https://doi.org/10.1016/0021-9290(75)90075-5

Tang, T., Cripton, P.A., Guy, P., McKay, H.A., Wang, R., 2018. Clinical hip fracture is accompanied by compression induced failure in the superior cortex of the femoral neck. Bone 108, 121–131. https://doi.org/10.1016/j.bone.2017.12.020

Wang, F., Yang, J., Miller, K., Li, G., Joldes, G.R., Doyle, B., Wittek, A., 2016. Numerical investigations of rib fracture failure models in different dynamic loading conditions. Computer Methods in Biomechanics and Biomedical Engineering 19, 527–537. https://doi.org/10.1080/10255842.2015.1043905

Yang, K., Lynch, M., O'Donnell, C., 2011. "Buckle" rib fracture: An artifact following cardio-pulmonary resuscitation detected on postmortem CT. Legal Medicine 13, 233–239. https://doi.org/10.1016/j.legalmed.2011.05.004

Yoganandan, N., Pintar, F.A., 1998. Biomechanics of Human Thoracic Ribs. Journal of Biomechanical Engineering 120, 100–104. https://doi.org/10.1115/1.2834288

Supplementary materials:

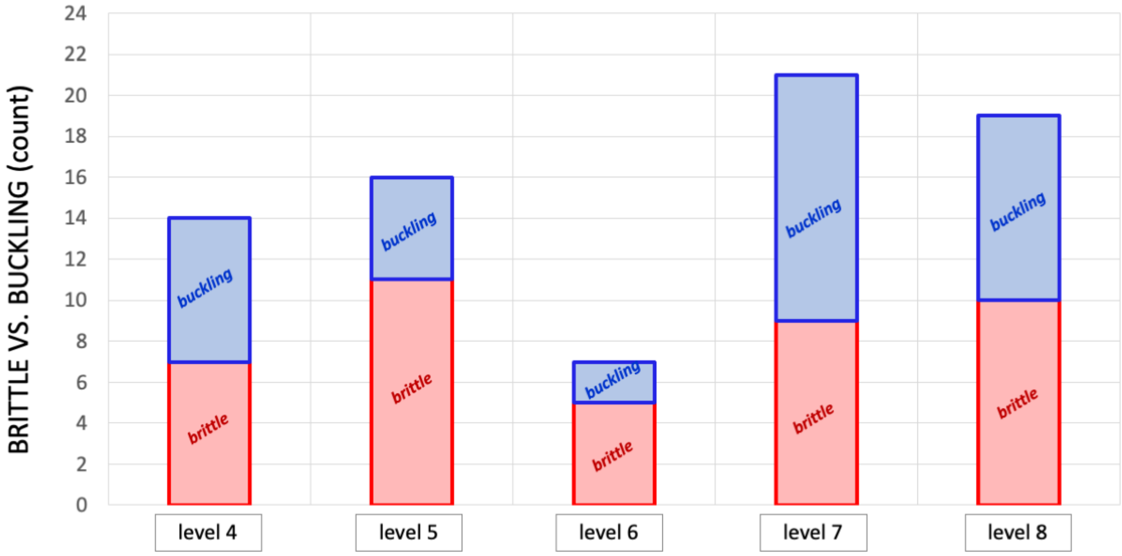

Fig. S1. Different mechanisms of fracture (brittle vs buckling) for the single rib levels. The red columns represent the count of the ribs fractured in brittle mode while the blue columns represent the ribs fractured in buckle mode.

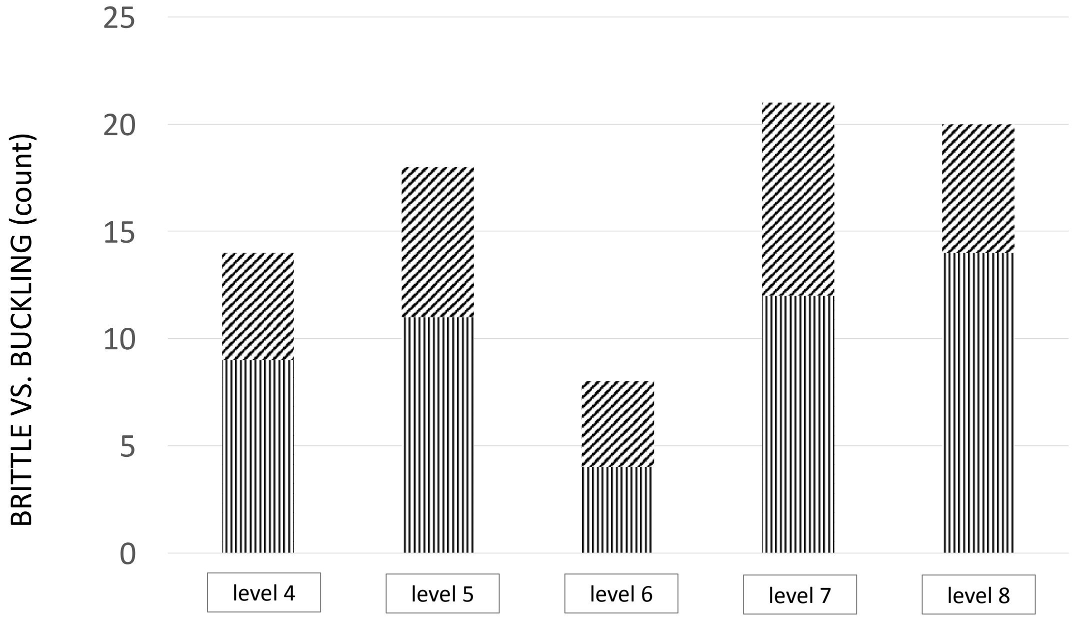

Fig. S2. Different principal strain directions (aligned vs oblique) for the single rib levels. The columns with the aligned pattern represent the ribs with aligned principal strain direction, while the columns with the oblique pattern represent the ribs with oblique principal strain direction.

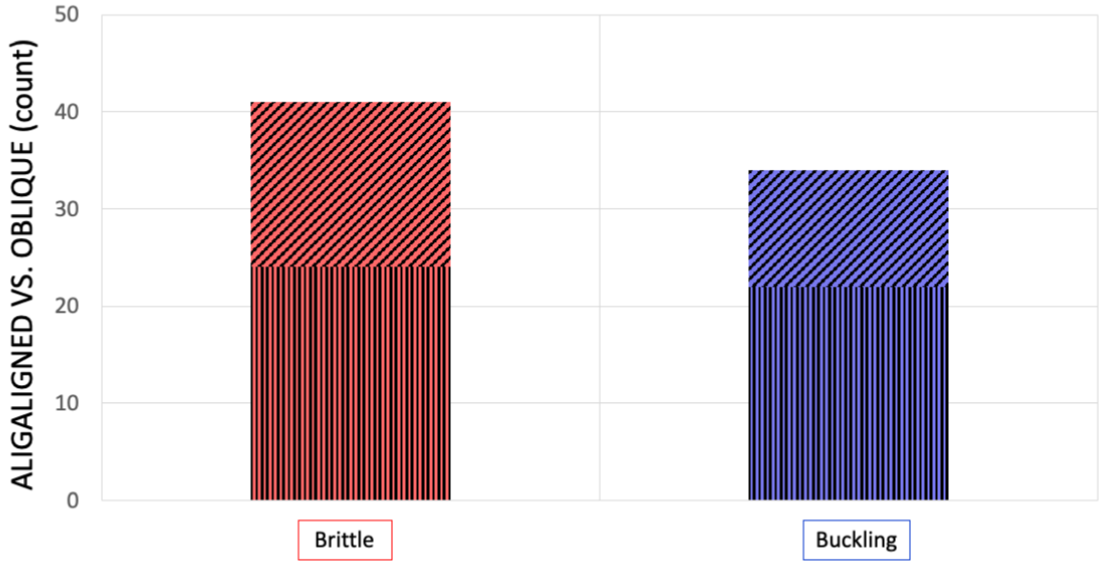

Fig. S3. Binning of the mechanisms of failure with respect to the principal strain direction. The red column represents the ribs that fractured in brittle mode while the blue column represents the ribs that fractured in buckling mode. Each column was divided in the proportion of ribs with aligned principal strain direction (aligned pattern of the column) and the ribs with the oblique principal strain direction (oblique pattern of the column).

Table S1.

Data used for the statistical analysis reported in Table 3 of the main text.

Each sheet contains the data for the comparison between the reported physical entities (column 'Analysis' of Table 3 of the main text).